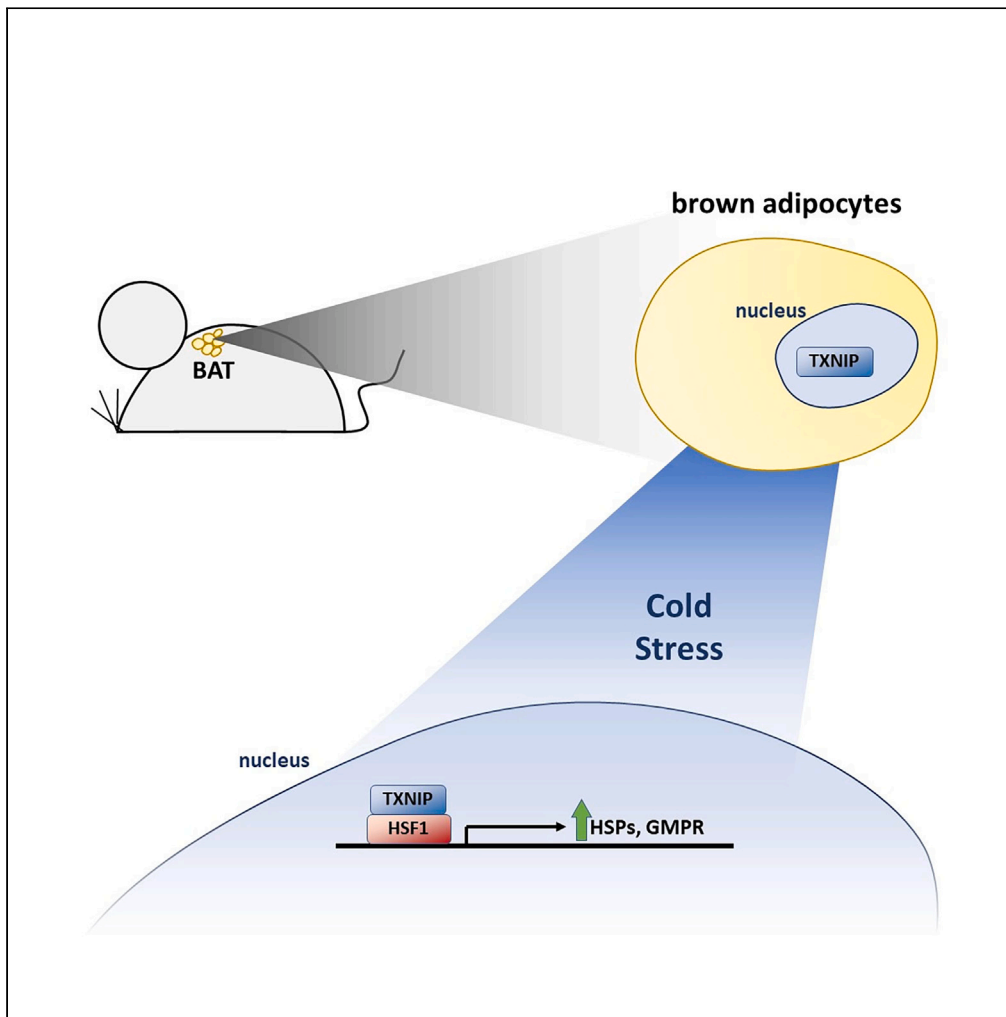


## Article

## Optimal HSF1 activation in response to acute cold stress in BAT requires nuclear TXNIP



Althea N.  
Waldhart, Kin H.  
Lau, Holly Dykstra,  
Tracey Avequin,  
Ning Wu

ning@omnispaceemail.com

**Highlights**

TXNIP nuclear localization  
is dynamic

Multiple cell types contain  
nuclear TXNIP *in vivo*

Nuclear TXNIP is required  
for optimal activation of  
HSF1 by cold in BAT

Waldhart et al., iScience 26,  
106538  
May 19, 2023 © 2023 The  
Author(s).  
[https://doi.org/10.1016/  
j.isci.2023.106538](https://doi.org/10.1016/j.isci.2023.106538)

## Article

## Optimal HSF1 activation in response to acute cold stress in BAT requires nuclear TXNIP

Althea N. Waldhart,<sup>1</sup> Kin H. Lau,<sup>1</sup> Holly Dykstra,<sup>1</sup> Tracey Avequin,<sup>1</sup> and Ning Wu<sup>1,2,\*</sup>

## SUMMARY

While TXNIP (thioredoxin interacting protein) in the plasma membrane and vesicular location is known to negatively regulate cellular glucose uptake by facilitating glucose transporter endocytosis, the function of TXNIP in the nucleus is far less understood. Herein, we sought to determine the function of nuclear TXNIP *in vivo*, using a new HA-tagged TXNIP knock-in mouse model. We observed that TXNIP can be found in the nucleus of a variety of cells from different tissues including hepatocytes (liver), enterocytes (small intestine), exocrine cells (pancreas), and brown adipocytes (BAT). Further investigations into the role of nuclear TXNIP in BAT revealed that cold stress rapidly and transiently activated HSF1 (heat shock factor 1). HSF1 interaction with TXNIP during its activation is required for optimal HSF1 directed cold shock response in BAT.

## INTRODUCTION

TXNIP (thioredoxin interacting protein) is a  $\alpha$ -arrestin protein that facilitates the endocytosis of glucose transporters GLUT1 – 4.<sup>1,2</sup> As such, TXNIP is part of a cellular autoregulatory circuit for glucose uptake that minimally consists of the glucose transporter, TXNIP, and glucose-responsive transcription factors ChREBP/Mlx and MondoA/Mlx.<sup>3,4</sup> Too much glucose influx leads to ChREBP/Mlx or MondoA/Mlx translocating into the nucleus to drive *Txnip* transcription. The newly synthesized TXNIP protein binds to the glucose transporters to bring them into the cytoplasm via the clathrin-coated pathway, thus reducing glucose uptake. In response to energy starvation or growth factor stimulation, TXNIP is known to become phosphorylated on Ser308 by AMPK or AKT respectively, dissociating from the glucose transporters. This promptly stops the transporters endocytosis and leads to an acute increase in glucose uptake, making TXNIP an important AKT substrate downstream of insulin activation. In the absence of insulin stimulation, TXNIP ensures low levels of GLUT4 on the cell surface, while insulin stimulation promotes phosphorylation of TXNIP, stopping GLUT4 endocytosis and avoiding a futile GLUT4 trafficking cycle. Knocking out TXNIP results in fasting hypoglycemia, due to the high basal levels of glucose transporters on the cell surface, and consequently hyperlipidemia.<sup>5</sup>

The involvement of TXNIP in glucose transporter endocytosis is consistent with its location within the plasma membrane and vesicular location in cultured cells, as well as the hypoglycemic metabolic phenotypes observed in TXNIP knockout mice. However, in many cultured cell lines, TXNIP also exhibits a dominant nuclear localization that is believed to be related to importin  $\alpha$ 1-mediated TXNIP nuclear translocation.<sup>6</sup> Despite this observation, the nuclear functions of TXNIP, particularly *in vivo*, remain largely undetermined.

Herein, we report a series of experiments aimed at examining the nuclear functions of TXNIP, in part utilizing a new N-terminal HA-tagged TXNIP knock-in mouse model. We found that in cultured cells, TXNIP cellular location was very dynamic, translocating into the nucleus upon stress, but not in a way that correlated with its interaction with thioredoxin. *In vivo*, TXNIP was found in the nucleus of a variety of cells from different tissues including hepatocytes (liver), enterocytes (small intestine), exocrine cells (pancreas), and in brown adipocytes (brown adipocyte tissue [BAT]). In BAT, we found nuclear TXNIP was necessary for the optimal activation of HSF1 (heat shock factor 1) in response to acute cold stress. Together, these observations provide evidence that TXNIP may be an important coordinator between cellular stress and metabolic response.

## RESULTS

## Nuclear localization of TXNIP in cultured cells is dynamic

Previously, we observed nuclear localization of GFP-tagged TXNIP during live cell imaging in HepG2 cells.<sup>1,2</sup> Here, using suspension Hela S3 cells and hypotonic lysis, we showed that endogenous TXNIP could

<sup>1</sup>Van Andel Institute, Grand Rapids, MI 49503, USA

<sup>2</sup>Lead contact

\*Correspondence:

ning@omnispace.com

<https://doi.org/10.1016/j.isci.2023.106538>



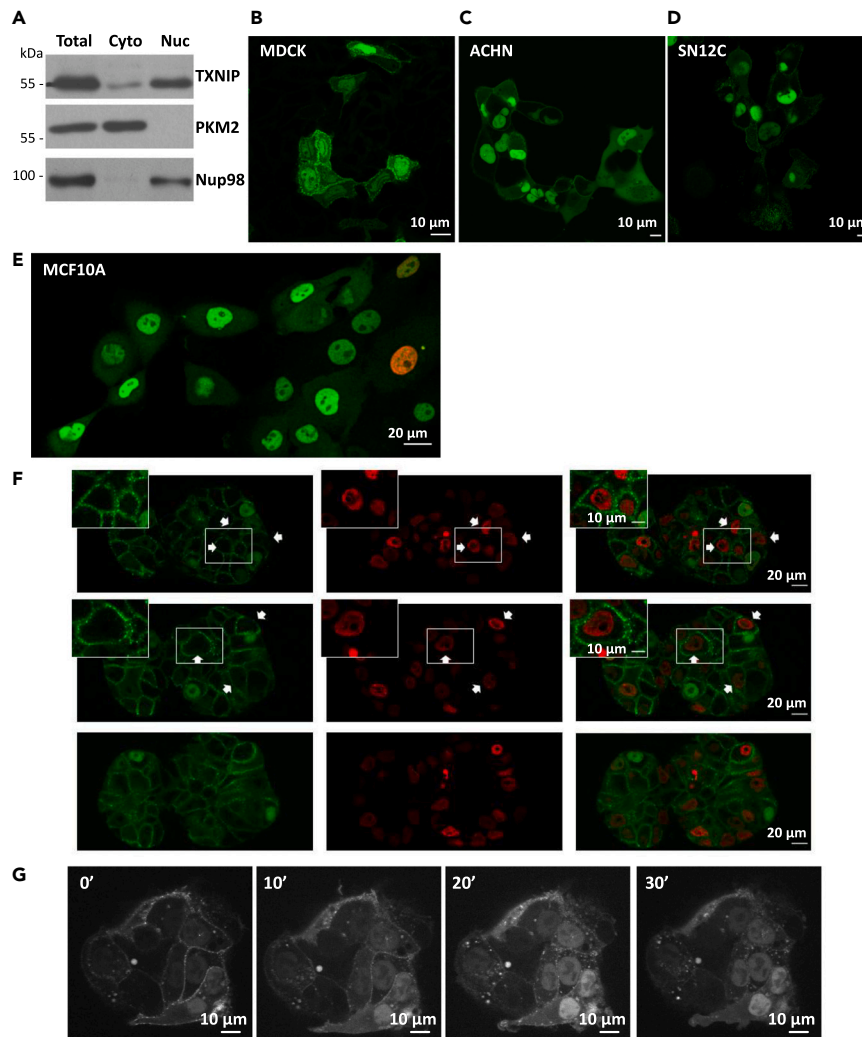


**Figure 1. TXNIP localization in cultured cell lines**

(A) Western blot of HeLa S3 cell fractionation showing TXNIP in nucleus. GFP-TXNIP localization (B) in MDCK cells, (C) in ACHN cells, and (D) in SN12C cells.

(E) MCF10A cells stably expressing GFP-TXNIP and Histone H2-mCherry grown in 2D.

(F) The same MCF10A cells from (E) grown as 3D clusters in Matrigel.

(G) Live cell imaging time course of HepG2/GFP-TXNIP cells treated with 100  $\mu$ M H<sub>2</sub>O<sub>2</sub>. (Also see [Figure S1](#)).

be found in the cell nuclear fraction ([Figure 1A](#)), indicating the nuclear location of TXNIP is neither a GFP-fusion nor an ectopic overexpression artifact. We verified that nuclear location of TXNIP was also present in other cell lines by stably expressing GFP-TXNIP in cell lines such as MDCK, ACHN, and SN12C ([Figures 1B–1D](#)). TXNIP nuclear localization has been reported by other groups as well.<sup>6,7</sup> We also noted that within the same cell line, TXNIP distributions could be dramatically different between individual cells. For example, some SN12C cells had GFP-TXNIP on their plasma membrane and in their nuclei, while others had more in the cytoplasm and less on the plasma membrane or in their nuclei. Given TXNIP's role in regulating glucose uptake in the plasma membrane, this location heterogeneity implies the glucose usage varies widely among individual cells even within the same population.

Further, we found that TXNIP cellular distribution was dependent on culturing conditions. When MCF10A cells that stably express GFP-TXNIP and histone 2B-mCherry were cultured on plastic in 2D, TXNIP was found mostly in their nuclei and cytoplasm ([Figure 1E](#)). However, when the same cells were grown in Matrigel as 3D clusters, the number of cells with nuclear TXNIP decreased and localization on their plasma

membrane and vesicles became much more prominent (Figure 1F). Scanning across the z axis using a confocal microscope, we could identify cells without any observable TXNIP in the nuclei at all (Figure 1F, white arrows). Clearly, the cellular environment, including the supporting matrix, directly influences TXNIP localization. However, even within these larger trends, the heterogeneity of TXNIP location among individual cells within the population remained.

In addition, we observed that TXNIP nuclear import can be triggered by H<sub>2</sub>O<sub>2</sub>. Using HepG2 cells stably expressing GFP-TXNIP and live-cell confocal imaging, 100 μM H<sub>2</sub>O<sub>2</sub> was observed to trigger GFP-TXNIP dissociation from the plasma membrane and accumulation in the nucleus within 20 min (Figure 1G). Since H<sub>2</sub>O<sub>2</sub> is an oxidant and TXNIP forms a disulfide-linked conjugate with thioredoxin (TXN) upon oxidation via Cys247,<sup>8</sup> we wondered whether the oxidation of Cys247 was necessary for nuclear translocation. Treating HepG2 cells stably expressing GFP-TXNIP-C247S mutant with H<sub>2</sub>O<sub>2</sub>, we still observed nuclear translocation of TXNIP (Figure S1). As such, residue 247 does not need to be oxidizable for TXNIP to be transported into the nucleus, and the formation of a TXNIP-TXN conjugate is not required for the transport process.

Collectively, these data demonstrate that TXNIP nuclear localization is a dynamic, regulated process in response to cellular environment.

### Nuclear localization of TXNIP *in vivo* in multiple tissues

Since nuclear TXNIP in cell lines was heterogeneous and dependent on culturing conditions, and since TXNIP expression is regulated by cell cycle,<sup>9</sup> we wanted to confirm whether TXNIP is found in the nucleus of terminally differentiated cells under normal physiological conditions *in vivo*. To facilitate our investigation, we created an HA-tagged TXNIP knock-in (KI) mouse line (from now on, we will refer to the tagged TXNIP protein as NTX). A double HAHA-tag was inserted right after TXNIP's initial Met residue with Ser-GlyGly as the linker peptide (Figure 2A). The inserted sequence was verified by PCR using primers flanking the inserted sequence (Figure S2A), by showing an upshift in alleles carrying the insertion, and by DNA sequencing (Figure S2B). After backcrossing the animals for at least 10 generations to eliminate potential off target mutations generated by CRISPR/cas9, we compared the expression level of NTX in various tissues of KI mice relative to their littermate matched WT animals by Western blot. Overall, KI mice expressed NTX at slightly higher levels than the WT mice expressed TXNIP (Figures 2B and S3). This increase in NTX protein did not seem to affect the general metabolism of the mice, as their body weights, fat content, and lean mass were not different from the WT animals (Figures 2C–2E). Fasting blood glucose and free fatty acids levels were also similar, with triacylglyceride levels trending higher in KI mice (Figures 2F–2H). Additionally, oral glucose boluses were cleared from the blood at the same speed as in the WT animals (Figures 2I and 2J) while fed and fasting insulin levels were also comparable between WT and KI animals (Figures 2K and 2L).

Next, we took advantage of the HA-tag to examine cellular NTX expression by immunohistochemistry (IHC). Here, we found dramatic differences in NTX expression in different cell types from different tissues. For example, in lung and breast tissues, we found very strong NTX expression in the ductal epithelium (Figures S4A and S4B). Even among this layer of cells, NTX levels differed from cell to cell, perhaps indicating different cell types within the epithelium or different metabolic state of cells as seen in tissue cultured cell lines. In addition, we observed strong NTX expression in Kupffer cells in the liver (Figure S4C) and in choroid plexus cells from the brain (Figure S4D). In the latter, NTX colocalized with GLUT1 on the basolateral membrane adjacent to blood capillaries. This differed from the rest of the brain, where TXNIP is minimally expressed and GLUT1 is highly expressed.<sup>5,10</sup> The brain's reliance on peripheral tissues such as the pancreas and liver to maintain blood glucose levels, without burdening itself with glucose entry regulation, may explain these findings. Further, NTX expression in the choroid plexus may reflect the dynamic energy needs for glucose in these cells, particularly given the energy required for secreting cerebral spinal fluid.

We also identified clear signs of nuclear NTX in the brown adipose tissue (BAT) (Figure 3A) and in the pancreas (Figure 3B). In BAT, NTX was visible in the cytoplasm and nuclei (big and round) of brown adipocytes. Some other smaller cells also exhibited significant NTX expression, but it was difficult to judge cellular localization due to their small cell size. In the pancreas, NTX showed stronger staining in exocrine cells (acinar cells) than in islet cells. By immunofluorescence (IF), we confirmed that islet cells with higher NTX expression were not α- or β-cells (Figures S5A and S5B). In addition, we found evidence of NTX nuclear

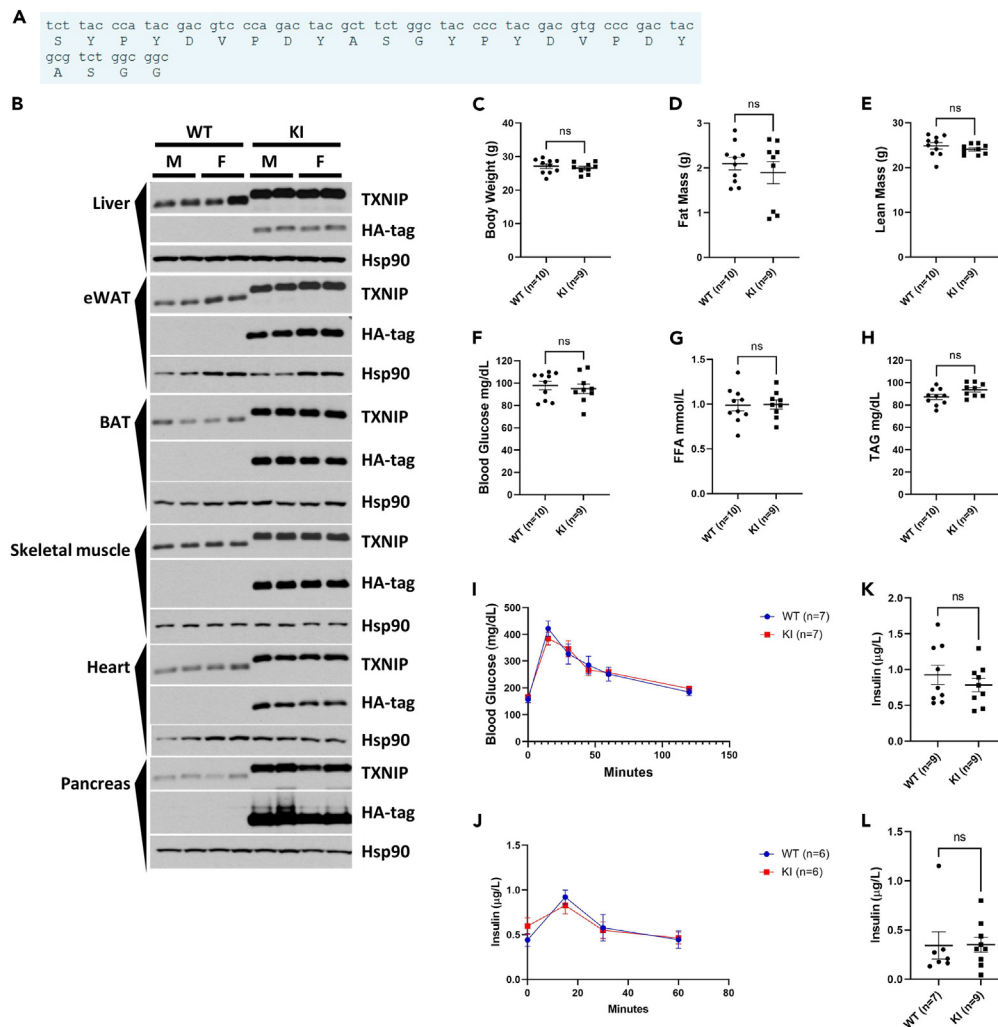


**Figure 2. Construction and metabolic characterization of KI mice**

(A) DNA and protein sequence of double HA-tag inserted at the N-terminus of TXNIP, right after the first Met.  
 (B) Western blots showing NTX protein expression level compared to WT in various tissues. NTX upshift is due to HA-tag. M = male, F = female. MW marker see Figure S3.  
 (C) Body weight, (D) fat mass, (E) lean mass, (F) fasting blood glucose, (G) fasting FFA, (H) fasting TAG levels of KI mice compared to WT mice.  
 (I) Blood glucose response and (J) insulin response of WT and KI mice in oral glucose tolerance test.  
 (K) Fed blood insulin level and (L) fasted blood insulin level of WT and KI mice.  
 (C–L) were done with male mice. Mean  $\pm$  SEM.) (Also see Figures S2 and S3).

localization in hepatocytes, as well as small intestine and spleen tissue by IF (Figures 3C–3E). In the liver, hepatocytes closer to the portal veins had increased nuclear NTX levels than cells close to the central vein (Figures 3C and S6). Given the previous H<sub>2</sub>O<sub>2</sub>-induced TXNIP nuclear translocation data in HepG2 cells, there may be a connection between the nuclear localization of NTX, the oxygen tension gradient, and the metabolic zonal differences in the liver.<sup>11–13</sup> The portal vein region has higher oxygenation tension than the central vein region, and correspondingly more TXNIP nuclear localization in hepatocytes located close to the portal vein. Both the immune cells in the spleen and enterocytes in the small intestine had clear plasma membrane localized NTX. In addition, just like in tissue cultured cells, one could clearly see nuclear NTX, which was excluded from DAPI-rich nucleoli, the site of ribosome biogenesis.<sup>14</sup>

Therefore, it is clear that TXNIP can localize to the nucleus in various terminally differentiated cell types *in vivo*, therefore, nuclear TXNIP likely play a role in cellular function outside cell cycle regulation.

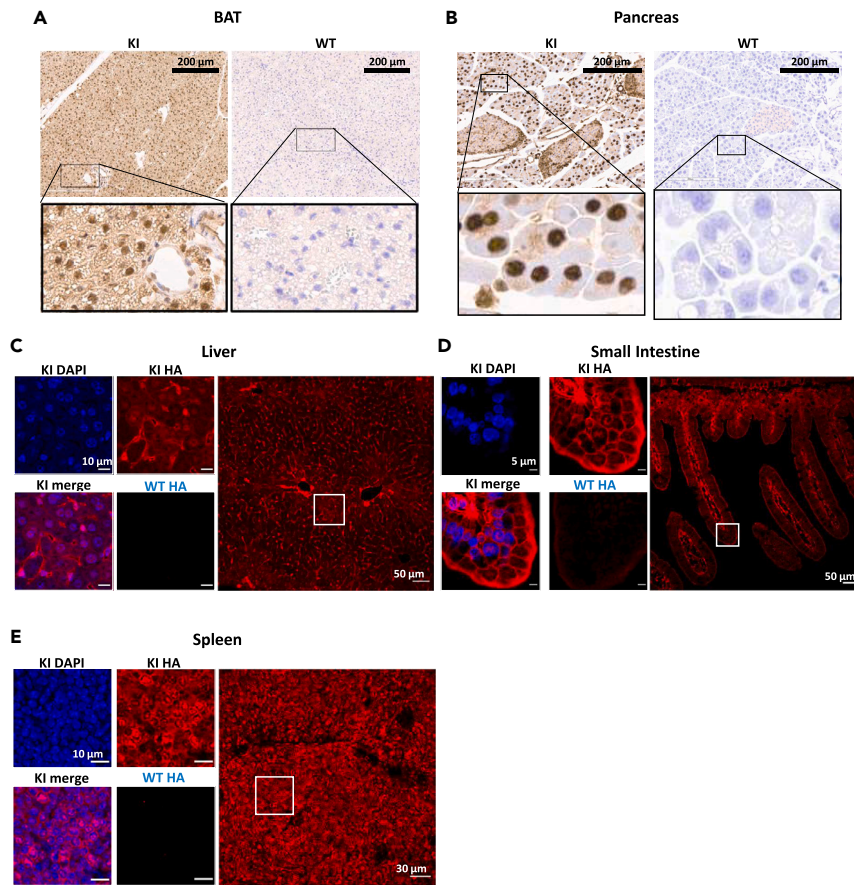


**Figure 3. NTX cellular location in KI tissues by IHC and IF**

(A) BAT IHC of KI and WT mice, using HA-tag antibody.

(B) Pancreas IHC of KI and WT mice, using HA-tag antibody. Confocal immunofluorescent images of liver (C), small intestine (D), and spleen (E) of KI mice using HA-tag antibody. (Also see [Figures S4–S6](#)).

### TXNIP interacts with HSF1 in BAT nuclei

Given our previous experience with BAT, we decided to focus our attention on determining the function of nuclear TXNIP in BAT.<sup>15</sup> The primary function of BAT is heat generation in order to maintain body temperature. During cold stress, norepinephrine from nerves stimulates adrenergic receptors in BAT, leading to a series of metabolic and gene transcription changes to increase the flux through the mitochondria.<sup>16</sup> During this time, AKT is activated, as shown by AKT 308 and 473 phosphorylation, as well as phosphorylation of its substrate FOXO1/3 ([Figure 4A](#)).<sup>17</sup> Activated AKT also phosphorylates TXNIP on S308, triggering increased glucose uptake as required for thermogenesis. In tissue cultured cells, phosphorylated TXNIP is subsequently degraded.<sup>2</sup> However, S308 phosphorylation in brown adipocytes did not seem to change the overall TXNIP protein level significantly, as shown by Western blots of the whole BAT ([Figures 4A and 4B](#)) and blot quantification ([Figure 4C](#)). This is because the TXNIP mRNA level did not change, permitting continuous TXNIP protein translation ([Figure S7A](#)). The level of nuclear TXNIP was not expected to be affected by AKT activation as we previously showed that AKT phosphorylation of TXNIP requires both proteins to co-localize to PI (3,4,5) P<sub>3</sub> containing membranes.<sup>1</sup> Indeed, quantification of staining of nuclear NTX by IF showed no change between brown adipocytes at RT and those that experienced either a 40min or 4h cold stress *in situ* ([Figures S7B and S7C](#)). This suggests that TXNIP has a stable presence in the nuclei of brown adipocytes.

We have also shown previously that knocking out TXNIP leads to a blunted BAT thermogenic response to acute cold stress, partly due to rigidification of the mitochondrial membrane.<sup>15</sup> The previous mRNAseq analysis also showed that cold stress upregulated transcription of heat shock protein (HSP) genes in WT

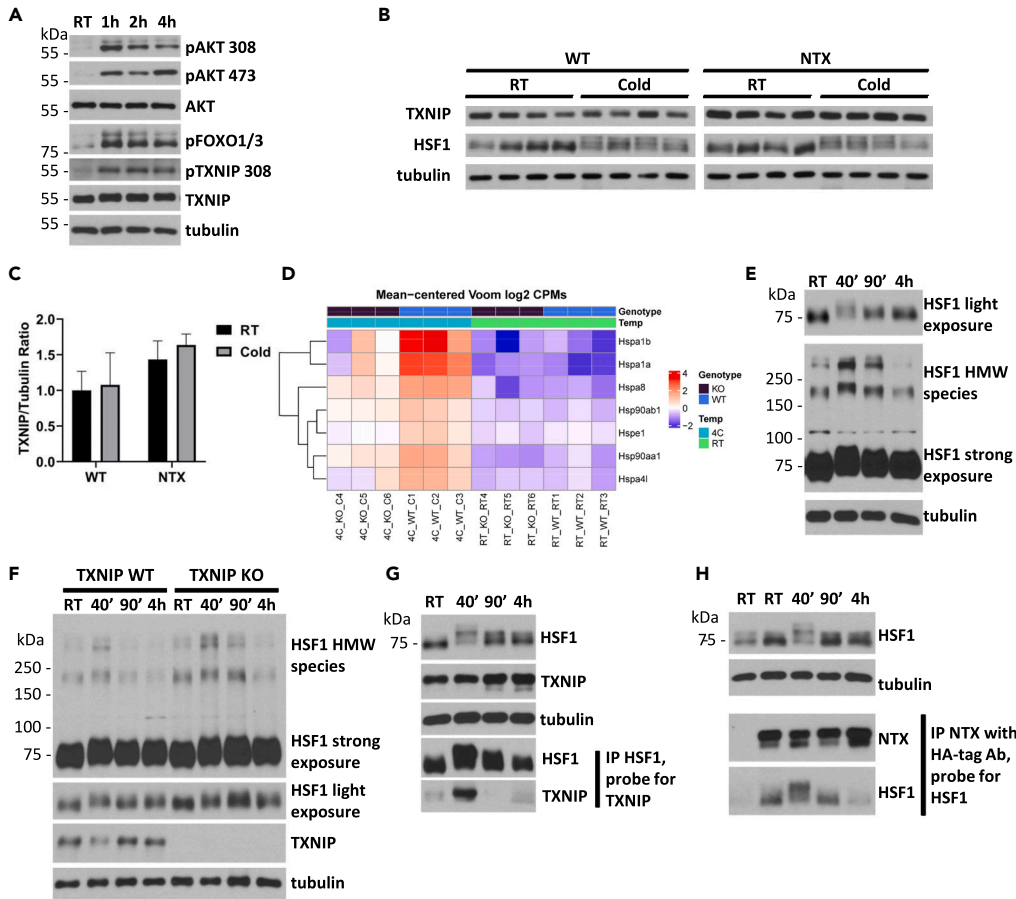


**Figure 4. TXNIP interaction with HSF1**

(A) Representative Western blots of BAT (total tissue lysates) of WT animals treated with indicated time of cold stress. (B) Western blot of TXNIP and HSF1 levels at RT and after 4 h of cold stress in BAT from WT and KI animals. (C) Quantification of blots in (B) (mean  $\pm$  SD). (D) Heatmap of heat shock protein genes that showed significantly reduced upregulation in TXNIP KO mice compared to WT. (E) Representative Western blot of total BAT lysates of WT animals treated with indicated time of cold stress and DSG crosslinking. HMW = high molecular weight species. (F) Western blots showing HSF1 activation by cold stress in TXNIP WT and KO BAT, DSG used (total tissue lysates). (G) Western blots of endogenous HSF1 IP (IP HSF1 probe for TXNIP) after DSP crosslinking, showing HSF1 and TXNIP interaction after 40min of cold stress. (H) Western blots of HA-tag IP from KI BAT (IP NTX, probe for HSF1) after DSP crosslinking, showing interaction between endogenous HSF1 and NTX protein. (Also see [Figure S7](#)).

animals, while many of these HSP gene transcriptional increases were significantly blunted in TXNIP KO ([Figure 4D](#)). Since heat shock factors (HSF) are the best known transcription factors regulating HSPs, we wanted to confirm whether nuclear TXNIP facilitates activation of HSF1, the best studied of the HSF, in the context of cold stress response in BAT. HSF1 activation by heat stress in cultured cells is fast, transient, and complex, involving post-translational modifications affecting HSF1 trimerization as well as binding to DNA.<sup>18–20</sup> The currently accepted model suggests that HSF1 exists as a monomer, complexed to HSPs under normal conditions. During heat stress, HSPs dissociate from HSF1 in order to bind other labile proteins. Concurrent post-translational modifications (PTMs) induced by heat shock allow for HSF1 trimer formation in the nuclei, and its interaction with DNA to activate transcription.

We carried out a series of short time course cold stress events at 40min, 90min, and 4h using crosslinker DSG (disuccinimidyl glutarate) as reported by others to detect HSF1 trimer formation.<sup>21</sup> BAT tissue was crosslinked at the time of harvest, before tissue lysis for Western blots. We observed increased trimer levels and more higher molecular weight (HMW) species after 40min of cold stress. However, the crosslinking

procedure was very inefficient as majority of HSF1 protein remained as monomer at 75 kDa. From these monomers, we found that HSF1 was most heavily modified after 40min of cold stress, resulting in an upshift in protein molecular weight on a Western blot (Figure 4E, HSF1 light exposure). HSF1 returned to pre-treatment states within 4h, both in regards to PTMs and trimer formation; this is consistent with the published, transient nature of HSF1 oligomerization.<sup>22,23</sup>

Given that the trimer formation is critical for DNA binding, we wanted to know if TXNIP is needed for HSF1 to form trimers. Using TXNIP WT and KO mice, we found no significant HSF1 trimer or higher molecular weight complex formation in the presence or absence of TXNIP (Figure 4F), and there was no convincing evidence of HSF1 PTMs being affected either. Next, we wanted to determine if there was physical interaction between HSF1 and TXNIP. Since we did not observe TXNIP in HSF1 HMW species by Western blot during our DSG crosslinking experiment (reprobing Figure 4E with TXNIP antibody), we switched to DSP (dithiobis[succinimidyl propionate]) because its crosslinking can be reversed by reducing agents and this would let us see interactions more clearly in the crosslinked protein population using immunoprecipitation. With DSP crosslinking, we did observe a strong interaction between HSF1 and TXNIP upon immunoprecipitation of TXNIP using the HSF1 antibody in wild-type animals (Figure 4G), or immunoprecipitation of HSF1 using HA-tag antibody in NTX animals (Figure 4H). In both cases, the interaction was strongest after 40min of cold stress. Just like TXNIP, we did not observe changes in HSF1 nuclear localization by IHC between RT and 40min of cold stress (Figures S7D and S7E), consistent with previous reports that the activation of HSF1 by heat stress does not require cytoplasm-to-nucleus translocation.<sup>24</sup> These results suggest that TXNIP and HSF1 interaction happens in the nuclei of brown adipocytes between TXNIP and HSF1 that is already present in the nuclei before treatment and that this interaction is strongest immediately after cold stress.

### Transient increase of HSF1 binding to DNA after cold stress

Heat shock response has traditionally been studied in cellular responses to increases in temperature. Our previous Western blots showed that HSF1 is also activated after cold stress in BAT, as indicated by increases in PTMs and trimerization levels. To investigate if these changes correlate with increased HSF1 interaction with DNA and gene expression, we performed HSF1 ChIPseq in replicates of BAT from wild-type mice at RT after 40min and after 4h of cold stress at 4°C. In mice at RT, BAT was partially activated because it was below the thermoneutral temperature of mice. Our analysis found HSF1 bound to 788 sites at RT (Figure S8A). This value increased to 1460 sites after 40min of cold stress, decreasing to only 101 sites after 4h of cold stress.

HOMER (Hypergeometric Optimization of Motif EnRichment) known motif analysis showed that half of the observed binding sites contained the heat shock response motif (Figure S8B). Most of the binding sites are located in the promoter and intragenic region of genes (Figure 5A). HSF1 DNA binding is highest after 40min cold stress, akin to its modifications and oligomerization. These observations are illustrated by the average peak size (counts per million) and peak heatmaps at the 3 time points (Figure 5B), as well as the differential binding analysis (Figure 5C). The average peak size is highest after the 40min cold shock, indicating the strongest HSF1 and DNA interaction. The M2 plot showed a general increase in DNA binding from RT to 40min of cold stress (pink average line above 0), as well as 520 peaks with significant increases in size (pink dots, FDR < 0.050). Interestingly, the activation of HSF1 was largely terminated after 4h of cold stress. That is, although these animals were still experiencing cold temperature, HSF1 had dissociated from the DNA resulting in even less DNA binding observed after 4h of cold stress than at RT. Analysis showed that the DNA sites with increased HSF1 binding after 40min are also the sites with decreased HSF1 binding after 4h (Figure 5D). This could also be seen by examining the peak heights (fold enrichment of reads in ChIP samples over the input sample) of the top HSF1 DNA binding sites at each time point (Table S1). The top binding site both before and after cold stress is the shared promoter region between *Hspd1* and *Hspe1*. At this site, binding increases going from RT to 40min of cold shock and then clearly decreases from 40min to 4h (Figure 5E).

Typically, transcription factors binding in the promoter or intragenic regions of a gene are thought to regulate the gene expression. Here, we identified genes that have HSF1 bound in their promoters and/or intragenic regions after 40min of cold stress, and ran pathway analysis using GSEA (Gene Set Enrichment Analysis) with these genes. The top pathways showing significant enrichment are all involved in the cellular response to heat stress (Figure 5F). However, not all genes with HSF1 bound in these regions show significantly increased mRNA expression (Figure 5G). This trend was similar to what has been observed previously in HSF1 response

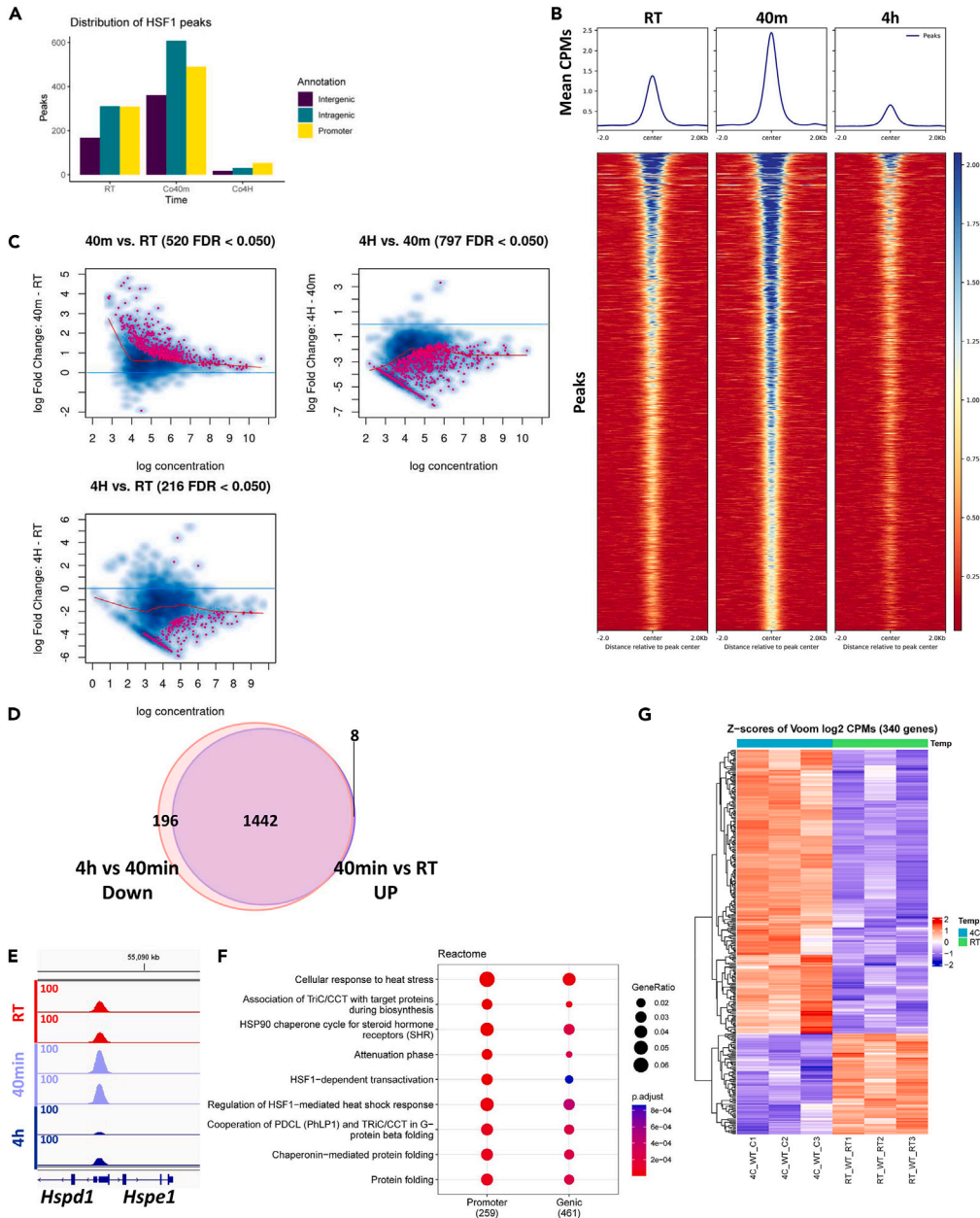


**Figure 5. HSF1 fast and transient binding to DNA during cold stress**

(A) HSF1 binding site location distribution.  
 (B) Average HSF1 ChIPseq peak heights and peak size distribution heatmap of the 3 time points: RT, 40min, and 4h after cold stress.  
 (C) M2 plots of HSF1 binding pairwise comparison among the 3 time points.  
 (D) Venn diagram showing the increase in HSF1-DNA interaction from RT to 40min after cold stress is at the same DNA sites as the decrease going from 40min to 4h.  
 (E) HSF1 DNA binding pattern at *Hspd1* and *Hspe1* promoter region.  
 (F) GSEA pathway analysis of the genes with HSF1 binding at their promoter (promoter alone) or genic (either promoter or intragenic) region at 40min of cold stress.  
 (G) mRNA expression heatmap of genes with HSF1 bound in their genic region, as well as significant expression difference between RT and 4h cold stress. (Also see [Figure S8](#) and [Table S1](#)).

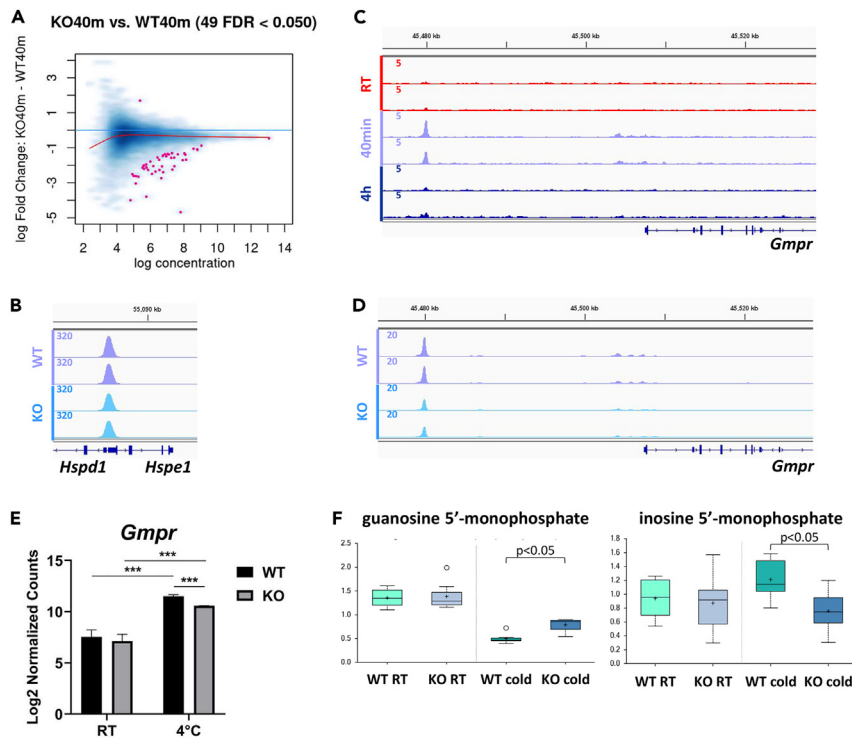


**Figure 6. Reduced HSF1 activation in TXNIP KO BAT in response to cold**

(A) M2 plot of TXNIP WT and KO HSF1 ChIPseq peaks after 40min of cold stress.  
 (B) HSF1 peak profile comparison between TXNIP WT and KO at the promoters of *Hspd1* and *Hspe1*.  
 (C) HSF1 peak profile upstream of *Gmpr* at RT, 40min, and 4h after cold stress.  
 (D) HSF1 peak profile comparison between TXNIP WT and KO upstream of *Gmpr* after 40min of cold stress.  
 (E) mRNA level of *Gmpr* in TXNIP WT and KO BAT before and after 4h of cold stress,  $n = 3$ , mean  $\pm$  SD.  
 (F) GMP and IMP levels in TXNIP WT and KO BAT before and after 4h of cold stress, mean  $\pm$  SD. (Also see Figure S9 and Table S2).

to heat stress in cell lines.<sup>20</sup> This is understandable since these genes may be under control of multiple transcription factors, not just HSF1.

### HSF1 transcriptional activity modulation by TXNIP

Since the strongest interaction between HSF1 and DNA is after 40min of cold stress, we wondered whether the delayed response in heat shock protein mRNA upregulation in TXNIP KO is due to a delayed binding of HSF1 to DNA. As such, we carried out BAT HSF1 ChIPseq in TXNIP WT and KO after 40min of cold stress in replicates. We identified 10206 shared peaks for WT and 7879 shared peaks for KO (Figure S9). Consistent with less peaks in KO, the M2 plot showed a general decrease in the interaction between HSF1 and DNA in the KO mice relative to WT animals (Figure 6A). This observation held for all the heat shock protein genes that exhibited differential upregulation after 40min of cold shock in BAT from TXNIP KO mice (Figure 4D and Table S2). The *Hspd1* and *Hspe1* shared promoter peak was among the peaks where the decrease from WT to KO was significant (pink dot in Figures 6A and 6B).

A peak upstream of *Gmpr* stood out among the significantly different WT and KO peaks. Similar to the *Hspd1/Hspe1* peak, this *Gmpr* peak also showed dramatic upregulation at 40min of cold stress compared to RT and downregulation after 4h of cold stress (Figure 6C). This peak was also smaller in KO mice relative to WT animals after 40min of cold stress (Figure 6D). Increased *Gmpr* mRNA levels after cold stress provided further support for the idea that the HSF1 binding site actually regulates *Gmpr* expression (Figure 6E). As GMPR carries out the NADPH-dependent deamination of GMP to IMP, increased GMPR protein levels would be expected to shift the intracellular balance of nucleotides from G toward A, which is the energy

source for proper functioning of the heat shock proteins. Using metabolomics, we found decreased GMP and increased IMP levels in WT mice after 4h of cold stress, while these changes are significantly decreased in KO mice (Figure 6F). Together, these data imply that HSF1 not only regulates heat shock proteins themselves, but that it also participates in regulating the metabolites needed for proper functioning of these same heat shock proteins. In addition, TXNIP is required for optimal HSF1 activation on a subset of heat shock response genes.

## DISCUSSION

TXNIP is a multifunctional protein. Its regulation of glucose transporter trafficking best matches the observed hypoglycemic and hyperlipidemia metabolic phenotype in KO mice. However, its nuclear localization, often observed in cultured cells, has long been a functional mystery, especially as TXNIP nuclear localization has been observed to be highly dynamic. Even within cells from a single population, localization of TXNIP varies within the cell. Changing growth conditions from 2D to 3D can reduce TXNIP nuclear localization, while stressing cells with H<sub>2</sub>O<sub>2</sub> can induce membrane TXNIP to translocate to the nucleus. Clearly, TXNIP is acutely responsive to cellular environment. In an attempt to examine the nuclear function of TXNIP *in vivo*, we generated HA-tagged knock-in mice to identify the cell types that have nuclear TXNIP in the context of normal physiology. Given the sensitivity of TXNIP to cellular environment in cultured cells, the tissue fixing process needed to be quick to accurately capture TXNIP membrane localization. The clearest TXNIP plasma membrane localization was found in the small intestine, where we could fix the tissue within minutes by flushing the fixative directly through the small intestine. If we assume these few minutes cause least amount of fixation artifacts, then TXNIP can be present on the plasma membrane, as well as in the nucleus at the same time in the enterocytes. We do not know if there are physiological perturbations that can induce plasma membrane TXNIP to translocate into the nucleus in various cell types like we observed for the artificial H<sub>2</sub>O<sub>2</sub> treatment of HepG2 cells. Even though we believe that there is glucose/metabolic requirement change associated with many types of cellular perturbations with TXNIP serving as a dual glucose regulator and stress responder, much work is needed to confirm and validate the details of such a mechanism. We suspect each cell type/tissue must be studied separately under its own types of physiologically possible stress.

Because of our previous work in BAT, and the clear nuclear location of TXNIP in BAT, we decided to investigate the nuclear function of TXNIP in BAT. In doing so, we found transcription factor HSF1 activation, most often studied in the context of heat stress is modulated by TXNIP. In BAT thermogenesis, the brown adipocytes generate heat that is quickly carried away by increased blood flow through BAT. It is easy to imagine that the brown adipocytes, themselves, are under transient heat stress initially, which triggers HSF1 activation. Our data suggest that HSF1 activation is fast and transient, in alignment with previous studies in the HSF1 field, with the greatest activation observed after 40min of cold stress and waning after 4h of cold stress. We found strong TXNIP-HSF1 interaction at the time point of highest HSF1 activation, alluding to the necessity of TXNIP association for maximum HSF1 activation. Since we had to use crosslinkers to show HSF1/TXNIP interaction by immunoprecipitation, this may not be a direct interaction. Further work is needed to elucidate the mechanistic details of this interaction and its consequences. For example, one would need PRO-seq data at 40min of cold stress to pinpoint the exact gene set controlled by HSF1, and proteomics experiments to differentiate between different dynamic protein complexes. Given the importance of TXNIP in regulating GLUT4 endocytosis in insulin response,<sup>1</sup> this new insight on HSF1 regulation provides a potential connection between glucose metabolism and the protein folding response caused by cold stress that consumes ATP in brown adipocytes.

We also observed strong TXNIP expression within immune cells in multiple tissues. Due to the smaller size of the immune cells, such as Kupffer cells in the liver, it was difficult to discern TXNIP cellular location. However, we clearly observed both plasma membrane and nuclear localization of TXNIP in cells from the spleen. Since immune cells are designed for quick action, high levels of TXNIP expression in immune cells may allow for a dynamic range of immune response, keeping inactivated cells quiescent by reducing surface GLUT1 levels, while still maintaining their readiness for full activation without having to make more GLUT1 protein. HSF1 function in immune response has been documented previously,<sup>25,26</sup> and it will be interesting to see if TXNIP also modulates HSF1 function in the immune response context. More broadly, TXNIP's role in immune metabolism may shed light on mechanisms connecting obesity and its associated impaired immune response.<sup>27</sup>

Overall, we confirmed nuclear localization of TXNIP has its own function, separate from its role in glucose transport. Whether HSF1 is the only effector or if multiple effectors exist in different tissue and cell types requires further investigation. Regardless, the HA-TXNIP (NTX) knock-in mouse strain will be a good tool for future mechanistic studies *in vivo* searching for the missing functional link between the two spatial pools of TXNIP.

### Limitations of the study

There are a number of limitations to this study. (1) Using fixed tissue to study NTX localization by either IHC or IF depends on the speed of fixation. The fixation process itself may cause artifacts, such as causing TXNIP to fall off membranes. Creative handling of the tissue is likely necessary for further investigation. (2) Inserting HA-tag at the N-terminus of TXNIP changes protein level relative to WT through an unknown mechanism. Further metabolic characterization to study phenotypes, such as potentially higher TAG in KI mice may need to construct tissue specific KI models.

### STAR★METHODS

Detailed methods are provided in the online version of this paper and include the following:

- KEY RESOURCES TABLE
- RESOURCE AVAILABILITY
  - Lead contact
  - Materials availability
  - Data and code availability
- EXPERIMENTAL MODEL AND SUBJECT DETAILS
- METHOD DETAILS
  - Tagged knock-in mice construction
  - OGTT
  - Cold stress
  - Histology
  - Nuclear localization of Hsf1 methods
  - Immunofluorescence staining
  - Nuclear NTX imaging and quantification methods
  - Western blots
  - Immunoprecipitation with DSP
  - qPCR
  - ChIPseq
  - Bioinformatics
  - Metabolomics
- QUANTIFICATION AND STATISTICAL ANALYSIS

### SUPPLEMENTAL INFORMATION

Supplemental information can be found online at <https://doi.org/10.1016/j.isci.2023.106538>.

### ACKNOWLEDGMENTS

The authors thank the VAI vivarium staff for maintaining the mice colonies, VAI transgenic core for generating the NTX mice, and the VAI genomics core facility for providing excellent facilities and services. N.W. is supported by National Institute of Health grant R01-GM120129.

### AUTHOR CONTRIBUTIONS

N.W. conceived the idea and designed the experiments. A.N.W. maintained the mice colonies and carried out mice phenotyping experiments. K.L. did all of the bioinformatic analysis. H.D. and T.A. helped with IHC, IF, and image quantification.

### DECLARATION OF INTERESTS

The authors declare no competing interests.

Received: December 5, 2022

Revised: February 4, 2023

Accepted: March 24, 2023

Published: April 10, 2023

## REFERENCES

- Waldhart, A.N., Dykstra, H., Peck, A.S., Boguslawski, E.A., Madaj, Z.B., Wen, J., Veldkamp, K., Hollowell, M., Zheng, B., Cantley, L.C., et al. (2017). Phosphorylation of TXNIP by AKT mediates acute influx of glucose in response to insulin. *Cell Rep.* 19, 2005–2013. <https://doi.org/10.1016/j.celrep.2017.05.041>.
- Wu, N., Zheng, B., Shaywitz, A., Dagon, Y., Tower, C., Bellinger, G., Shen, C.H., Wen, J., Asara, J., McGraw, T.E., et al. (2013). AMPK-dependent degradation of TXNIP upon energy stress leads to enhanced glucose uptake via GLUT1. *Mol. Cell* 49, 1167–1175. <https://doi.org/10.1016/j.molcel.2013.01.035>.
- Uyeda, K., Yamashita, H., and Kawaguchi, T. (2002). Carbohydrate responsive element-binding protein (ChREBP): a key regulator of glucose metabolism and fat storage. *Biochem. Pharmacol.* 63, 2075–2080.
- Stoltzman, C.A., Peterson, C.W., Breen, K.T., Muoio, D.M., Billin, A.N., and Ayer, D.E. (2008). Glucose sensing by MondoA: Mlx complexes: a role for hexokinases and direct regulation of thioredoxin-interacting protein expression. *Proc. Natl. Acad. Sci. USA* 105, 6912–6917. <https://doi.org/10.1073/pnas.0712199105>.
- Bodnar, J.S., Chatterjee, A., Castellani, L.W., Ross, D.A., Ohmen, J., Cavalcoli, J., Wu, C., Dains, K.M., Catanese, J., Chu, M., et al. (2002). Positional cloning of the combined hyperlipidemia gene *Hyp1p1*. *Nat. Genet.* 30, 110–116. <https://doi.org/10.1038/ng811>.
- Nishinaka, Y., Masutani, H., Oka, S.I., Matsuo, Y., Yamaguchi, Y., Nishio, K., Ishii, Y., and Yodoi, J. (2004). Importin alpha1 (Rch1) mediates nuclear translocation of thioredoxin-binding protein-2/vitamin D(3)-up-regulated protein 1. *J. Biol. Chem.* 279, 37559–37565. <https://doi.org/10.1074/jbc.M405473200>.
- Patwari, P., Chutkow, W.A., Cummings, K., Verstraeten, V.L.R.M., Lammerding, J., Schreiter, E.R., and Lee, R.T. (2009). Thioredoxin-independent regulation of metabolism by the alpha-arrestin proteins. *J. Biol. Chem.* 284, 24996–25003. <https://doi.org/10.1074/jbc.M109.018093>.
- Patwari, P., Higgins, L.J., Chutkow, W.A., Yoshioka, J., and Lee, R.T. (2006). The interaction of thioredoxin with Txnip. Evidence for formation of a mixed disulfide by disulfide exchange. *J. Biol. Chem.* 281, 21884–21891. <https://doi.org/10.1074/jbc.M600427200>.
- Lee, H.J., Jedrychowski, M.P., Vinayagam, A., Wu, N., Shyh-Chang, N., Hu, Y., Min-Wen, C., Moore, J.K., Asara, J.M., Lyssiotis, C.A., et al. (2017). Proteomic and metabolomic characterization of a mammalian cellular transition from quiescence to proliferation. *Cell Rep.* 20, 721–736. <https://doi.org/10.1016/j.celrep.2017.06.074>.
- Oka, S.I., Masutani, H., Liu, W., Horita, H., Wang, D., Kizaka-Kondoh, S., and Yodoi, J. (2006). Thioredoxin-binding protein-2-like inducible membrane protein is a novel vitamin D3 and peroxisome proliferator-activated receptor (PPAR)gamma ligand target protein that regulates PPARgamma signaling. *Endocrinology* 147, 733–743. <https://doi.org/10.1210/en.2005-0679>.
- Jungermann, K., and Kietzmann, T. (1997). Role of oxygen in the zonation of carbohydrate metabolism and gene expression in liver. *Kidney Int.* 51, 402–412. <https://doi.org/10.1038/ki.1997.53>.
- Kietzmann, T. (2017). Metabolic zonation of the liver: the oxygen gradient revisited. *Redox Biol.* 11, 622–630. <https://doi.org/10.1016/j.redox.2017.01.012>.
- Cunningham, R.P., and Porat-Shliom, N. (2021). Liver zonation - revisiting old questions with new technologies. *Front. Physiol.* 12, 732929. <https://doi.org/10.3389/fphys.2021.732929>.
- Raska, I., Shaw, P.J., and Cmarko, D. (2006). Structure and function of the nucleolus in the spotlight. *Curr. Opin. Cell Biol.* 18, 325–334. <https://doi.org/10.1016/j.ceb.2006.04.008>.
- Waldhart, A.N., Muhire, B., Johnson, B., Pettinga, D., Madaj, Z.B., Wolfrum, E., Dykstra, H., Wegert, V., Pospisilik, J.A., Han, X., and Wu, N. (2021). Excess dietary carbohydrate affects mitochondrial integrity as observed in brown adipose tissue. *Cell Rep.* 36, 109488. <https://doi.org/10.1016/j.celrep.2021.109488>.
- Blondin, D.P., Nielsen, S., Kuipers, E.N., Severinsen, M.C., Jensen, V.H., Miard, S., Jespersen, N.Z., Kooijman, S., Boon, M.R., Fortin, M., et al. (2020). Human Brown adipocyte thermogenesis is driven by beta2-AR stimulation. *Cell Metab.* 32, 287–300.e7. <https://doi.org/10.1016/j.cmet.2020.07.005>.
- Sanchez-Gurmaches, J., Tang, Y., Jespersen, N.Z., Wallace, M., Martinez Calejman, C., Gujja, S., Li, H., Edwards, Y.J.K., Wolfrum, C., Metallo, C.M., et al. (2018). Brown fat AKT2 is a cold-induced kinase that stimulates ChREBP-mediated De Novo lipogenesis to optimize fuel storage and thermogenesis. *Cell Metab.* 27, 195–209.e6. <https://doi.org/10.1016/j.cmet.2017.10.008>.
- Gomez-Pastor, R., Burchfiel, E.T., and Thiele, D.J. (2018). Regulation of heat shock transcription factors and their roles in physiology and disease. *Nat. Rev. Mol. Cell Biol.* 19, 4–19. <https://doi.org/10.1038/nrm.2017.73>.
- Kmieciak, S.W., and Mayer, M.P. (2022). Molecular mechanisms of heat shock factor 1 regulation. *Trends Biochem. Sci.* 47, 218–234. <https://doi.org/10.1016/j.tibs.2021.10.004>.
- Mahat, D.B., Salamanca, H.H., Duarte, F.M., Danko, C.G., and Lis, J.T. (2016). Mammalian heat shock response and mechanisms underlying its genome-wide transcriptional regulation. *Mol. Cell* 62, 63–78. <https://doi.org/10.1016/j.molcel.2016.02.025>.
- Neef, D.W., Turski, M.L., and Thiele, D.J. (2010). Modulation of heat shock transcription factor 1 as a therapeutic target for small molecule intervention in neurodegenerative disease. *PLoS Biol.* 8, e1000291. <https://doi.org/10.1371/journal.pbio.1000291>.
- Chowdhary, S., Kainth, A.S., Pincus, D., and Gross, D.S. (2019). Heat shock factor 1 drives intergenic association of its target gene loci upon heat shock. *Cell Rep.* 26, 18–28.e5. <https://doi.org/10.1016/j.celrep.2018.12.034>.
- Jolly, C., Usson, Y., and Morimoto, R.I. (1999). Rapid and reversible relocalization of heat shock factor 1 within seconds to nuclear stress granules. *Proc. Natl. Acad. Sci. USA* 96, 6769–6774. <https://doi.org/10.1073/pnas.96.12.6769>.
- Mercier, P.A., Winegarden, N.A., and Westwood, J.T. (1999). Human heat shock factor 1 is predominantly a nuclear protein before and after heat stress. *J. Cell Sci.* 112, 2765–2774. <https://doi.org/10.1242/jcs.112.16.2765>.
- Gandhapadi, S.K., Murapa, P., Threlkeld, Z.D., Ward, M., Sarge, K.D., Snow, C., and Woodward, J.G. (2013). Heat shock transcription factor 1 is activated as a consequence of lymphocyte activation and regulates a major proteostasis network in T cells critical for cell division during stress. *J. Immunol.* 191, 4068–4079. <https://doi.org/10.4049/jimmunol.1202831>.
- Reyes, A., Navarro, A.J., Diethelm-Varela, B., Kalergis, A.M., and González, P.A. (2022). Is there a role for HSF1 in viral infections? *FEBS Open Bio* 12, 1112–1124. <https://doi.org/10.1002/2211-5463.13419>.
- Muscogiuri, G., Pugliese, G., Laudisio, D., Castellucci, B., Barrea, L., Savastano, S., and Colao, A. (2021). The impact of obesity on immune response to infection: plausible mechanisms and outcomes. *Obes. Rev.* 22, e13216. <https://doi.org/10.1111/obr.13216>.
- Li, H. (2013). Aligning sequence reads, clone sequences and assembly contigs with

- BWA-MEM. Preprint at arXiv. <https://doi.org/10.48550/arXiv.1303.3997>.
29. Faust, G.G., and Hall, I.M. (2014). SAMBLASTER: fast duplicate marking and structural variant read extraction. *Bioinformatics* 30, 2503–2505. <https://doi.org/10.1093/bioinformatics/btu314>.
  30. Li, H., Handsaker, B., Wysoker, A., Fennell, T., Ruan, J., Homer, N., Marth, G., Abecasis, G., and Durbin, R.; 1000 Genome Project Data Processing Subgroup (2009). The sequence alignment/map format and SAMtools. *Bioinformatics* 25, 2078–2079. <https://doi.org/10.1093/bioinformatics/btp352>.
  31. Zhang, Y., Liu, T., Meyer, C.A., Eeckhoute, J., Johnson, D.S., Bernstein, B.E., Nusbaum, C., Myers, R.M., Brown, M., Li, W., and Liu, X.S. (2008). Model-based analysis of ChIP-seq (MACS). *Genome Biol.* 9, R137. <https://doi.org/10.1186/gb-2008-9-9-r137>.
  32. Ramírez, F., Ryan, D.P., Grüning, B., Bhardwaj, V., Kilpert, F., Richter, A.S., Heyne, S., Dündar, F., and Manke, T. (2016). deepTools2: a next generation web server for deep-sequencing data analysis. *Nucleic Acids Res.* 44, W160–W165. <https://doi.org/10.1093/nar/gkw257>.
  33. Zerbino, D.R., Johnson, N., Juettemann, T., Wilder, S.P., and Flicek, P. (2014). WiggleTools: parallel processing of large collections of genome-wide datasets for visualization and statistical analysis. *Bioinformatics* 30, 1008–1009. <https://doi.org/10.1093/bioinformatics/btt737>.
  34. Ross-Innes, C.S., Stark, R., Teschendorff, A.E., Holmes, K.A., Ali, H.R., Dunning, M.J., Brown, G.D., Gojis, O., Ellis, I.O., Green, A.R., et al. (2012). Differential oestrogen receptor binding is associated with clinical outcome in breast cancer. *Nature* 481, 389–393. <https://doi.org/10.1038/nature10730>.
  35. Zhu, L.J., Gazin, C., Lawson, N.D., Pagès, H., Lin, S.M., Lapointe, D.S., and Green, M.R. (2010). ChIPpeakAnno: a bioconductor package to annotate ChIP-seq and ChIP-chip data. *BMC Bioinformatics* 11, 237. <https://doi.org/10.1186/1471-2105-11-237>.
  36. Yu, G., Wang, L.G., and He, Q.Y. (2015). ChIPseeker: an R/Bioconductor package for ChIP peak annotation, comparison and visualization. *Bioinformatics* 31, 2382–2383. <https://doi.org/10.1093/bioinformatics/btv145>.
  37. Heinz, S., Benner, C., Spann, N., Bertolino, E., Lin, Y.C., Laslo, P., Cheng, J.X., Murre, C., Singh, H., and Glass, C.K. (2010). Simple combinations of lineage-determining transcription factors prime cis-regulatory elements required for macrophage and B cell identities. *Mol. Cell* 38, 576–589. <https://doi.org/10.1016/j.molcel.2010.05.004>.
  38. Yu, G., Wang, L.G., Han, Y., and He, Q.Y. (2012). clusterProfiler: an R package for comparing biological themes among gene clusters. *OMICS* 16, 284–287. <https://doi.org/10.1089/omi.2011.0118>.
  39. Amemiya, H.M., Kundaje, A., and Boyle, A.P. (2019). The ENCODE blacklist: identification of problematic regions of the genome. *Sci. Rep.* 9, 9354. <https://doi.org/10.1038/s41598-019-45839-z>.
  40. Lawrence, M., Huber, W., Pagès, H., Aboyoun, P., Carlson, M., Gentleman, R., Morgan, M.T., and Carey, V.J. (2013). Software for computing and annotating genomic ranges. *PLoS Comput. Biol.* 9, e1003118. <https://doi.org/10.1371/journal.pcbi.1003118>.
  41. Durinck, S., Spellman, P.T., Birney, E., and Huber, W. (2009). Mapping identifiers for the integration of genomic datasets with the R/Bioconductor package biomaRt. *Nat. Protoc.* 4, 1184–1191. <https://doi.org/10.1038/nprot.2009.97>.

## STAR★METHODS

### KEY RESOURCES TABLE

REAGENT or RESOURCE	SOURCE	IDENTIFIER
<b>Antibodies</b>		
Ins1-488 (1:150 IF)	Proteintech	CL488-67668, RRID AB_2919515
Glucagon-488 (1:200 IF)	Proteintech	CL488-67286, RRID AB_2883402
HA-Tag	Cell Signaling Technology	3724, RRID: AB_1549585
Anti-rabbit Alexa Fluor 647 (1:500 IF)	Cell Signaling Technology	4414, RRID: AB_10693544
HSF1	Cell Signaling Technology	4356, RRID: AB_2120258
AKT	Cell Signaling Technology	4685, RRID: AB_2225340
AKT p308	Cell Signaling Technology	13038, RRID: AB_2629447
AKT p473	Cell Signaling Technology	4060, RRID: AB_2315049
FOXO1 pT24/FOXO3 pT32	Cell Signaling Technology	9464, RRID: AB_329842
TXNIP	Cell Signaling Technology	14715, RRID: AB_2714178
PMK2	Cell Signaling Technology	4053, RRID: AB_1904096
Nup98	Cell Signaling Technology	2598, RRID: AB_2267700
Tubulin	Sigma	T9026, RRID: AB_477593
<b>Chemicals, peptides, and recombinant proteins</b>		
Target Retrieval Solution, High pH	Agilent	K800421-2
Saponin	Sigma	47036-50G-F
Goat Serum	ThermoFisher	16210064
BSA	Sigma	A4503
Fluoromount-G	SouthernBiotech	0100-01
HBSS	Sigma	H1387-10X1L
16% Formaldehyde Solution	ThermoFisher Scientific	28906
DSG	Santa Cruz Biotech	sc-285455A
DSP	ThermoFisher Scientific	22585
Protein A magnetic beads	ThermoFisher Scientific	10001D
Protein G magnetic beads	ThermoFisher Scientific	10003D
RNAse A	Qiagen	19101
Protein K	ThermoFisher Scientific	EO0491
Matrigel	Corning	356234
Protein A Sepharose	Cytiva	17078001
<b>Critical commercial assays</b>		
MinElute PCR Purification Kit	Qiagen	28004
SuperScript™ VILO™ Master Mix	ThermoFisher Scientific	11755050
<b>Deposited data</b>		
HSF1 ChIPseq	GEO	GSE218516
<b>Experimental models: Cell lines</b>		
HepG2	ATCC	HB-8065
ACHN	ATCC	CRL-1611
MDCK	Prof. Lewis C. Cantley lab (Dana-Farber Cancer Institute)	

(Continued on next page)

**Continued**

REAGENT or RESOURCE	SOURCE	IDENTIFIER
SN12C	Prof. Lewis C. Cantley lab (Dana-Farber Cancer Institute)	
MCF10A	Prof. Lewis C. Cantley lab (Dana-Farber Cancer Institute)	

**Experimental models: Organisms/strains**

Mouse: B6;129-Txnipm1Rlee/J	The Jackson Laboratory	JAX: 016847
Mouse: B6.C-Tg(CMV-cre)1Cgn/J	The Jackson Laboratory	JAX: 006054
Mouse: C57B6/J	The Jackson Laboratory	JAX: 000664

**Oligonucleotides**

NTX genotyping forward primer	Eurofins	5'-GTTTCCAGAGTTTCTCCAGTTGCGGAAG
NTX genotyping reverse primer	Eurofins	5'-CTTACACACTTCCACTATTACCCGTCC

**Software and algorithms**

Nikon Elements v.	Nikon	<a href="https://www.microscope.healthcare.nikon.com/products/software/nis-elements">https://www.microscope.healthcare.nikon.com/products/software/nis-elements</a>
Huygens Professional Software	Scientific Volume Imaging (SVI)	<a href="https://svi.nl/Huygens-Professional">https://svi.nl/Huygens-Professional</a>
ImageJ	NIH	<a href="https://imagej.nih.gov/ij/">https://imagej.nih.gov/ij/</a>
Prism	GraphPad	<a href="https://www.graphpad.com/scientific-software/prism/">https://www.graphpad.com/scientific-software/prism/</a>
bwa v0.7.17	Li <sup>28</sup>	
SAMBLASTER v 0.1.24	Faust and Hall <sup>29</sup>	
SAMtools v1.9	Li et al <sup>30</sup>	
macs2 v2.2.7.1	Zhang et al <sup>31</sup>	
deepTools v3.4.3	Ramírez et al. <sup>32</sup>	
WiggleTools v1.2.11	Zerbino et al <sup>33</sup>	
DiffBind v3.2.7	Ross-Innes et al. <sup>34</sup>	
ChIPpeakAnno v3.26.4	Zhu et al. <sup>35</sup>	
ChIPseeker v1.28.3	Yu et al. <sup>36</sup>	
HOMER v4.11.1	Heinz et al <sup>37</sup>	
ClusterProfiler v4.0.5	Yu et al. <sup>38</sup>	
TrimGalore v0.6.0		<a href="https://github.com/FelixKrueger/TrimGalore">https://github.com/FelixKrueger/TrimGalore</a>

**Other**

Premium Glass Coverslips, 24x40mm	Fisher Scientific	Cat#125485J
-----------------------------------	-------------------	-------------

**RESOURCE AVAILABILITY**

**Lead contact**

Further information and requests for resources and reagents should be directed to and will be fulfilled by the lead contact Ning Wu ([ning@omnispace.com](mailto:ning@omnispace.com)).

**Materials availability**

The HA-tagged TXNIP mice will be available from JAX.

**Data and code availability**

HSF1 ChIPseq data generated during this study are publicly available at GEO as GSE218516.

No new code was generated.

No other new unique reagent was generated.

Any additional information required to reanalyze the data reported in this paper is available from the [lead contact](#) upon request.

## EXPERIMENTAL MODEL AND SUBJECT DETAILS

Mice were maintained in a barrier facility in accord with the Institute's regulations for animal care and handling (IACUC 21-04-012). Strains *Txnip* flox/flox (JAX 016847) and CMV-Cre (JAX 006054) were purchased from the Jackson Laboratory. The total KO (CMV-Cre) mice were generated by crossing *Txnip* flox/flox with CMV-cre mice. The Cre transgene was bred out during the process. The KO mice were backcrossed to C57B6/J (JAX 000664) for over 10 generations. Mice were maintained on LabDiet 5010 (calorie composition: 28.7% from protein, 12.7% from fat, and 58.2% from carbohydrate). Unless indicated, mice of both sexes were used.

## METHOD DETAILS

### Tagged knock-in mice construction

CRISPR component design, procurement, and injection were performed by the VAI transgenic core (RRID SCR\_022914). Sequence information for the target locus was downloaded from [Ensembl.org](#). The 40 bp surrounding the KI integration point were analyzed for CRISPR guide sequences using [crispor.tefor.net](#) and [deepfh.com/#/cas9](#). Guide selection was based on proximity to the integration point, predicted cutting ability and specificity score. The repair template consisted of the knock-in tag sequence with 60–70 bp arms of homology on either side, which was ordered as a single-stranded ultramer from IDT. Guides were ordered as crRNA from IDT along with tracrRNA and Alt-R S.p. Cas9 nuclease V3 protein. (crRNA: GAACCCACUCGGCUCAAUCAGUUUUAGAGCUAUGCU, universal tracer RNA: AGCAUAGCAAGUU AAAAU AAGGCUAGUCCGUUAUCAACUUGAAAAAGUGGCACCGAGUCGGUGCUUU) Upon arrival, the template and guide components were resuspended to 1 µg/µL in 0.02 µm filtered IDTE before storage at –80°C. The Cas9 protein was stored undiluted at –20°C. Complete CRISPR mix was prepared the morning of injection. Equimolar amounts of crRNA and tracrRNA were duplexed in a thermocycler by first heating to 95°C, then cooling to 25°C over the course of ~20min. Cas9 protein was diluted to 2 µg/µL in 0.02 µm filtered IDTE, then added to the duplexed guides and left at room temperature for 10min to allow protein:–guide complexes to form. Temp late molecule was then added to yield an injection solution of final concentration 15 ng/µL duplexed guides, Cas9 protein and ultramer repair template in 0.02 µm filtered IDTE. Founder mice were screened by genotyping (forward primer 5'-GTTTCCAGAGTTTCTCCA GTTGCGGAAG, reverse primer 5'-CTTCACACACTTCCACTATTACCCGTCC) and sequencing. Mice were backcrossed to C57B6/J for 10 generations before used for experiments.

### OGTT

2 to 3 months old male WT and KI mice were fasted from 7 a.m. to 1:30 p.m. A bolus of glucose at 2 g/kg was delivered via oral gavage. Blood was sampled via the tail vein at various time points. Blood glucose was measured with Accu-Chek (Aviva).

Lean mass and fat mass were measured with an EchoMRI-4n1-500 system.

Tissue TAG was measure with Infinity Triglyceride kit from ThermoFisher Scientific. FFA was measured with NEFA-HR2 kit from FujiFilm.

### Cold stress

For experiments, male mice between 2 and 3 months old were used. To cold stress the mice, each mouse was placed in a paper bucket with some food, but no bedding, and then was placed in the cold room for the indicated length of time, with a typically start from 9 a.m. before sacrifice by cervical dislocation and collection of BAT for ChIP or Western.

### Histology

Tissue was fixed with 4% formaldehyde in PBS for 48h and sent to VAI histology core for embedding. Deparaffinization and antigen retrieval performed on Dako PT link platform using Dako High pH retriever buffer for 20 min at 97°C. Staining performed utilizing Dako Autostainer Link 48, utilizing Dako Rabbit Polymer HRP for secondary for 20min following primary antibody incubation for 30min. DAB detection

performed using Dako EnVision Flex Chromagen for 10min and Dako Flex Hematoxylin for 5min. Aperio scanning of slides was performed utilizing Leica Aperio AT2 system.

### Nuclear localization of Hsf1 methods

HSF1 nuclear localization was measured in 9 randomly selected fields per experiment. ImageJ software (NIH, Bethesda, MD) was used to quantitate the number of nuclei that were stained in each experimental condition. Hsf1-stained nuclei were divided by the total number of nuclei to yield the percent of HSF1 in BAT nuclei under each condition.

### Immunofluorescence staining

IHC slides underwent deparaffinization and antigen retrieval in Van Andel histology core using the Agilent Target Retrieval Solution, High pH, for Dako PT Link, at 97°C for 20min. These slides were then washed in TBS-T and immersed for 10min at room temperature (RT) in 0.1% Saponin/PBS to permeabilize tissue. After brief washing in TBS-T, tissue was blocked in 5% goat serum/2% BSA/PBS for 1 h at RT in a humidity chamber. After brief washing in TBS-T, slides received primary antibody (Ab) diluted in 1% BSA/PBS and incubated overnight in a humidity chamber at 4°C. Slides were washed with TBS-T the following day and then incubated with secondary Ab and DAPI diluted in 1% BSA/PBS for 1h at RT in the dark. After washing twice with TBS-T and twice with PBS, the tissue was covered with Fluoromount-G mounting medium and a glass coverslip and allowed to solidify for 2h, then sealed with clear nail polish. Once dry, the slides were stored at 4°C in the dark until imaging could be performed using the Nikon A1plus-RSi Laser Scanning Confocal Microscope (Melville, NY) and Nikon Elements acquisition. Laser power, pinhole size, and gain were consistent across samples. All images were deconvolved with Huygens Professional Software (Scientific Volume Image; The Netherlands).

### Nuclear NTX imaging and quantification methods

Fluorescence images were taken using a Nikon A1plus-RSi laser scanning confocal microscope under a 20x objective. Images were collected with consistent pinhole size, detector gain, and laser power settings. Deconvolution was performed using Huygens Professional Software (SVI, Hilversum, Netherlands). Mean fluorescent intensities (MFIs) were measured in 8 randomly selected fields per experiment. Nuclear NTX MFI was quantified using DAPI-stained regions to mark the nucleus and measuring HA fluorescence intensity across those regions using ImageJ software (NIH, Bethesda, MD).

### Western blots

After treatment, mice were sacrificed by cervical dislocation and intrascapular BAT was dissected out and frozen immediately in liquid nitrogen and stored at –80°C. Frozen tissues were lysed in RIPA buffer (30 mM Tris 7.5, 120 mM NaCl, 1 mM vanadate, 20 mM NaF, 1% NP40, 1% deoxycholate, 0.1% SDS), plus protease inhibitors and calyculin A. The clarified supernatant was used for running Western blots.

For detecting HSF1 oligomers, BAT tissue was dissected out, minced in fixative buffer (HBSS pH 7.5, 2 mM DSG (disuccinimidyl glutarate) and fixed with rotation for 25 min at RT. The reaction was terminated with addition of Tris 7.5 buffer (final 320 mM). The tissue pieces were spun down and washed one time with 50 mM Tris 7.5, 150 mM NaCl, frozen in liquid nitrogen, and stored in –80°C for later processing as above. The Western blot sample buffer included 2% 2-mercaptoethanol as standard reducing agent.

### Immunoprecipitation with DSP

BAT tissue was minced in buffer (HBSS pH 7.5, 2 mM DSP (dithiobis(succinimidyl propionate)), crosslinked for 25 min at RT, and reactions stopped with Tris 7.5. The tissue was lysed with a combination of mechanical grinding and 1% NP40. The lysate was cleared with bench top centrifugation and protein A agarose beads were added for 1 h to pre-clear the mouse antibodies. Then antibodies were added for overnight IP at 4°C. The second day, protein A beads were added to precipitate the antibodies for 1h. The beads were then washed 3 times with 50 mM Tris 7.5, 150 mM NaCl and 0.5% NP40 buffer. SDS-PAGE sample buffer with 50 mM DTT was added to the washed beads and samples heated at 100°C for 5min to un-crosslink the complexes before running Western blots. Input samples were un-crosslinked the same way.

### qPCR

Total RNA from BAT was extracted with the PureLink™ RNA mini kit (Invitrogen 12183018A). For qPCR, total RNA was reverse-transcribed into cDNA using Super-Script IV Vilo Mastermix (Invitrogen). Primers used for *Txnip*: forward 5'-TGT GAA GTT ACC CGA GTC AAA GC, reverse 5'-AGC GCA AGT AGT CCA AAG TCT. For statistics, an unpaired Student's *t* test was performed using GraphPad Prism version 8.00 for Windows, GraphPad Software, La Jolla California USA.

### ChIPseq

After cold stress, BAT tissue was dissected out (~2 months old male mice used), minced in fixative buffer (HBSS pH 7.5, 2 mM DSG (disuccinimidyl glutarate) and fixed with rotation for 25 min at RT. Then formaldehyde was added to a final 0.8% concentration and the tissue pieces were further fixed for 12 min at RT. The reaction was terminated with addition of Tris 7.5 buffer (final 320 mM). The tissue pieces were spun down and washed one time with 50 mM Tris 7.5, 150 mM NaCl, frozen in liquid nitrogen, and stored in  $-80^{\circ}\text{C}$  for later processing.

Frozen tissue was mechanically lysed using an electric tissue homogenizer in 50 mM Tris 8.0, 2 mM EDTA. SDS was added to a final 1% concentration. The lysate was rotated at  $4^{\circ}\text{C}$  for 15min, then sonicated using Diagenode Bioruptor UCD-200, 5" on and 5" off, for 3 cycles of 3min on low setting. The sonicated lysate was cleared with a maximum speed spin in a cold bench top centrifuge for 10min. The clarified lysate was diluted 10 times with ChIP wash buffer 1 (25 mM Tris 7.5, 5 mM  $\text{MgSO}_4$ , 100 mM KCl, 10% glycerol, and 0.1% NP40). The potassium-SDS precipitate was spun out at 4000g for 10min 1% of the lysate was saved as input before antibodies were added for binding overnight at  $4^{\circ}\text{C}$ . The next day, 1:1 mixture of protein A and protein G Dynabeads were added for 2h. Then the beads were washed 3 times with ChIP wash buffer 1, 1 time with ChIP wash buffer 2 (25 mM Tris 7.5, 5 mM  $\text{MgSO}_4$ , 300 mM KCl, 10% glycerol, and 0.1% NP40) and 3 times with TE (10 mM Tris 8.0, 1 mM EDTA) before eluted with 30 mM Tris 7.5, 1% SDS. NaCl was added to the ChIP samples and input samples to a final 0.6 M concentration, and un-crosslinking was carried out in a  $65^{\circ}\text{C}$  water bath overnight. The next day, 1  $\mu\text{L}$  RNAse A was added to each sample and the samples were incubated at  $57^{\circ}\text{C}$  for 45min, followed by incubation with proteinase K at  $65^{\circ}\text{C}$  for 45min. The final DNA was purified with the Qiagen MinElute PCR purification kit and submitted to the VAI genomics core for library construction and sequencing.

Libraries for input and immunoprecipitated samples were prepared by the Van Andel Genomics Core from 10 ng of input material and all available IP material using the KAPA Hyper Prep Kit (v5.16) (Kapa Biosystems, Wilmington, MA USA). Prior to PCR amplification, end repaired and A-tailed DNA fragments were ligated to uniquely barcoded dual indexes (IDT, Coralville, IA USA). Quality and quantity of the finished libraries were assessed using a combination of Agilent DNA High Sensitivity chip (Agilent Technologies, Inc.), QuantiFluor dsDNA System (Promega Corp., Madison, WI, USA), and Kapa Illumina Library Quantification qPCR assays (Kapa Biosystems). 50 bp, paired-end end sequencing was performed on an NovaSeq6000 sequencer using an S2, 100 bp sequencing kit (Illumina Inc., San Diego, CA, USA). Inputs were sequenced to a minimum of 60M reads and IPs to a minimum of 40M reads. Base calling was done with Illumina RTA3 and output of NCS was demultiplexed and converted to FastQ format with Illumina Bcl2fastq v1.9.0.

### Bioinformatics

ChIP-seq reads were trimmed to remove low-quality bases and adapter sequences using TrimGalore v0.6.0 (<https://github.com/FelixKrueger/TrimGalore>) with default settings. Trimmed reads were aligned to the GRCm38.p6 reference genome from GENCODE vM24 using bwa mem v0.7.17,<sup>28</sup> marking duplicates using SAMBLASTER v 0.1.24.<sup>29</sup> Alignments were filtered using SAMtools view v1.9<sup>30</sup> with the parameters '-q 30 -F 2828' and '-f 2'. For peak calling, alignments were additionally filtered using SAMtools view with the parameter '-F 1024' to remove duplicate reads. Peaks were called using 'callpeak' in MACS2 v2.2.7.1<sup>31</sup> using the parameters, "-f BAMPE -g 'mm' -q 0.05 --keep-dup 'all'" and specifying the corresponding input samples using the "-c" parameter. Called peaks were filtered if they overlapped with the ENCODE blacklist v2.<sup>39</sup>

Bigwig files were generated using the bamCoverage tool in deepTools v3.4.3<sup>32</sup> using the parameters, "--binSize 10 --extendReads --normalizeUsing 'CPM' --samFlagExclude 1024 --samFlagInclude 64" and "--blackListFileName" to specify the ENCODE blacklist v2. To generate Bigwig files representing the mean across replicates, wiggletools v 1.2.11<sup>33</sup> was used to calculate the mean values in Wiggle format, which were converted back to BigWig using wigToBigWig in UCSC tools. Read coverage heatmaps at

peaks were generated using the averaged Bigwig files and peaksets merged across replicates, as described in the section below; 'computeMatrix reference-point' from Deeptools was run with the parameters, "-b 2000 -a 2000 -missingDataAsZero -binSize 10" and specifying the ENCODE blacklist v2 using the "-bl" parameter, followed by running plotHeatmap. Motif enrichment analyses were run on the peaksets merged across replicates; the 'findMotifGenome.pl' script in HOMER v4.11.1<sup>37</sup> was run with the parameters, "-size 200 -mask" using the preconfigured 'mm10' genome.

Peaksets were imported into R v4.1.0 as GenomicRanges v1.44.0.<sup>40</sup> Peak overlap Venn diagrams were performed using the 'makeVennDiagram()' function in ChIPpeakAnno v3.26.4<sup>35</sup> with the parameter, "connectedPeaks = 'merge'"; peaksets corresponding to the Venn diagram intersections were obtained using the 'findOverlapsOfPeaks()' function, again setting "connectedPeaks = 'merge'". Annotation of peaks was performed using the 'annotatePeak()' function in ChIPseeker v1.28.3<sup>36</sup> with the parameter, "tssRegion = c(-3000, 500)". Pathway enrichment analyses were conducted using clusterProfiler v4.0.5,<sup>38</sup> using the default adjusted p value cutoff of 0.05. MSigDB gene set collections were downloaded using the msigdb v7.5.1. Differential binding was tested using DiffBind v3.2.7.<sup>34</sup> Read counting was done using the 'dba.count()' function with the parameters, "summits = DB\_summits, bUseSummarizeOverlaps = TRUE", and normalization was done using the 'dba.normalize' function with "normalize = DBA\_NORM\_NATIVE, background = TRUE". For contrasts, litter was included as a blocking variable if the dataset consisted of mice from multiple litters, and a significance cutoff of FDR <0.05 was used.

Heat shock genes were based on the human annotations (<https://www.genenames.org/data/genegroup/#!/group/582>) and were converted to mouse homologs using biomaRt v2.48.3<sup>41</sup> and the December 2021 Ensembl archive (<https://dec2021.archive.ensembl.org/>).

### Metabolomics

Polar metabolites analysis was done by Metabolon Inc. (<https://www.metabolon.com/>). Isolated BAT tissue was snap-frozen in liquid nitrogen and shipped to Metabolon.

### QUANTIFICATION AND STATISTICAL ANALYSIS

Unless otherwise stated, graphs and statistical significance were conducted with GraphPad Prism using unpaired two-tailed Student's t test for calculating P-values for pair-wise comparison.